Intrinsic Nonlinear Hall Detection of the Néel Vector for Two-Dimensional Antiferromagnetic Spintronics

Jizhang Wang,[1] Hui Zeng,[2] Wenhui Duan,[2,3,4,5] and Huaqing Huang[1,5,6,*]
[1]School of Physics, Peking University, Beijing 100871, China
[2]State Key Laboratory of Low-Dimensional Quantum Physics, Department of Physics, Tsinghua University, Beijing 100084, China
[3]Institute for Advanced Study, Tsinghua University, Beijing 100084, China
[4]Frontier Science Center for Quantum Information, Beijing 100084, China
[5]Collaborative Innovation Center of Quantum Matter, Beijing 100871, China
[6]Center for High Energy Physics, Peking University, Beijing 100871, China

(Received 22 December 2022; revised 29 April 2023; accepted 30 June 2023; published 31 July 2023)

The respective unique merit of antiferromagnets and two-dimensional (2D) materials in spintronic applications inspires us to exploit 2D antiferromagnetic spintronics. However, the detection of the Néel vector in 2D antiferromagnets remains a great challenge because the measured signals usually decrease significantly in the 2D limit. Here we propose that the Néel vector of 2D antiferromagnets can be efficiently detected by the intrinsic nonlinear Hall (INH) effect which exhibits unexpected significant signals. As a specific example, we show that the INH conductivity of the monolayer manganese chalcogenides MnX (X = S, Se, Te) can reach the order of nm $\cdot$ mA/V^2, which is orders of magnitude larger than experimental values of paradigmatic antiferromagnetic spintronic materials. The INH effect can be accurately controlled by shifting the chemical potential around the band edge, which is experimentally feasible via electric gating or charge doping. Moreover, we explicitly demonstrate its 2π-periodic dependence on the Néel vector orientation based on an effective $k \cdot p$ model. Our findings enable flexible design schemes and promising material platforms for spintronic memory device applications based on 2D antiferromagnets.

DOI: 10.1103/PhysRevLett.131.056401

Introduction.—The desire to reduce the size and power consumption of spintronic devices stimulated the emergence of a new field referred to as two-dimensional (2D) spintronics [1–6]. Two-dimensional materials with atomic thickness have attracted extraordinary interest in spintronics because they not only provide a promising opportunity to push the relevant devices to the 2D limit, but also enable the hopeful exploration of new spintronic phenomena due to their unusual spin-dependent properties, such as the spin-valley coupling of transition metal dichalcogenides [7] and the spin-momentum locking of quantum spin Hall insulators [8]. However, almost all the existing 2D materials proposed for spintronics are nonmagnetic or ferromagnetic [9] (e.g., CrI_3 [10] and $CrGeTe_3$ [11]). In this Letter, we extend the 2D spintronics to antiferromagnets and show that the Néel vector, which serves as a state variable for 2D antiferromagnetic spintronics, can be detected by the nonlinear Hall measurement.

Antiferromagnets composed of antiferromagnetically coupled magnetic elements are attractive for spintronics because of their faster dynamics, zero stray fields, and insensitivity to magnetic perturbations [12–14]. The robust high-speed manipulation of the Néel vector [15,16], such as ultrafast 90° switching by current-induced spin-orbit torque [17–22] and reproducible 180° reversal by flipping the polarity of the writing current [23,24], have been demonstrated in recent experiments. However, the failure of Néel vector detections via conventional magnetic techniques due to the absence of net magnetization poses a major challenge for practical applications of antiferromagnetic spintronics [12]. Several optical and microscopic methods, such as the spin-polarized scanning tunneling microscopy [25], the x-ray magnetic linear dichroism microscopy [26], the femtosecond pump-probe magneto-optical experiment [27], the spatially resolved second-harmonic generation [28,29], and the diamond nitrogen-vacancy scanning probe magnetometry [30] work for accurate detection of the Néel vector. The anisotropic magnetoresistance (AMR) effect is useful for experimental detection of a 90° rotation but is invariant upon a 180° reversal of the Néel vector, and its small magnitude limits the readout speed and the possible miniaturization [31]. Recently, the reversed Néel vector states have been electrically distinguished by a second-order magnetoresistance effect [24,32,33], but have been limited in bulk materials. Since the readout speed and size scalability are usually proportional to the magnitude of the response signal which could significantly diminish in the ultimate atomic limit [13,34], it is, therefore, natural to raise the question: how to efficiently detect the Néel vector with a significantly large readout signal for 2D antiferromagnetic spintronics?

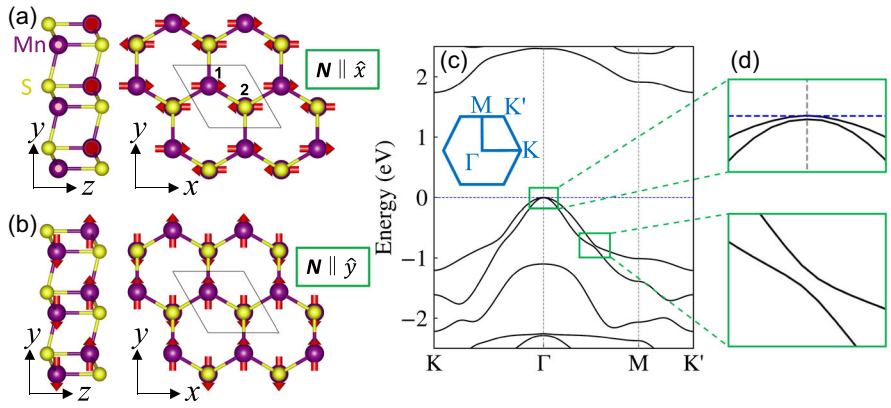

FIG. 1. Atomic and band structure of MnS. (a),(b) The top and side view of monolayer MnS with $\boldsymbol{N}\|\hat{x}$ and $\boldsymbol{N}\|\hat{y}$. Red arrows indicate magnetic moments. (c) The band structure of MnS with $\boldsymbol{N}\|\hat{x}$. The insert shows the Brillouin zone. (d) The enlarged plot of bands in small-gap regions.

In this Letter, we predict that the Néel vector of 2D antiferromagnets can be efficiently read out using the intrinsic nonlinear Hall (INH) effect which exhibits a significant signal that can be detected by experimental means. Taking 2D manganese chalcogenide MnX (X = S, Se, Te) as an example, we show that the INH conductivity of the MnS monolayer can reach the order of nm · mA/V^2, which is orders of magnitude larger than the experimentally measured values of typical antiferromagnets CuMnAs [24,32] and Mn_2Au [33]. The INH effect can be controlled by shifting the chemical potential via electric gating or charge doping. We further develop an effective $k \cdot p$ model to explain its dependence on the Néel vector direction with a 2π periodicity. Together with the efficient write-in approach based on current-induced spin-orbit torques, our findings constitute promising design schemes and material platforms for 2D antiferromagnetic spintronics.

Atomic and band structures.—Owing to similar crystal structures of 2D MnX, which have been successfully synthesized in experiments [35], we take MnS as an example hereafter and defer the rest to the Supplemental Material [36]. As shown in Fig. 1(a), MnS crystallizes in an AA-stacked bilayer honeycomb lattice, where Mn (and X) atoms on the top and bottom layers (Mn_1 and Mn_2) occupy opposite sublattices. The lattice structure belongs to the space group of $P\bar{3}m1$ (No. 164, D_{3d}^3). Our first-principles calculations [36] show that the magnetic moments are 4.36 μ_B per Mn and are antiferromagnetically ordered, which are consistent with previous studies [47]. The Néel vector $\boldsymbol{N}$, defined as the difference of the magnetic moments between Mn_1 and Mn_2 in the unit cell, shows significant in-plane anisotropy with the magnetocrystalline anisotropy energy being 0.4 meV/unit cell. For $\boldsymbol{N}$ lying in different in-plane directions, there is little energy difference (see Fig. S5 in the Supplemental Material [36]), indicating that it is possible to electrically manipulate $\boldsymbol{N}$ by current pulses via spin-orbit torques [19,24,48,49]. Importantly, for any arbitrary direction of $\boldsymbol{N}$ denoted by the polar angle θ with respect to the x axis, the spatial and time-reversal symmetry combination ($\mathcal{PT}$) is preserved.

Figure 1(c) shows the band structure for 2D MnS with $\boldsymbol{N}\|\hat{x}$. Because of the $\mathcal{PT}$ symmetry, every band is doubly degenerate. It is noted that some nearly degenerate points (NDPs) lie at Γ at the valence band maximum and along the Γ-M line around $E \approx -0.8$ eV. Since the valence bands are dominated by the S-p orbitals, the weak spin-orbit coupling (SOC) of S only induces slight band splitting at the NDPs [see Fig. 1(d)] compared with MnSe and MnTe [36], which plays a crucial role for the INH effect, as we will discuss later.

INH effect in MnS.—In general, the nonlinear Hall conductivity tensor is defined as the quadratic current response $\boldsymbol{J}$ to electric field $\boldsymbol{E}$: $J^\alpha = \sum_{\beta\neq\alpha,\gamma} \sigma^{\alpha\beta\gamma} E^\beta E^\gamma$, where α, β, γ are Cartesian indices. The nonlinear Hall conductivity can be separated into time-reversal-even ($\mathcal{T}$-even) and $\mathcal{T}$-odd parts, but only the latter can be utilized to detect the Néel vector reversal. In 2D antiferromagnets respecting the $\mathcal{PT}$ symmetry, the $\mathcal{T}$-even Berry curvature dipole (BCD) contribution σ_{BCD} is strictly forbidden [50,51]. In contrast, the $\mathcal{T}$-odd INH conductivity σ_{INH} which is allowed becomes an ideal quantity for the Néel vector detection, and is therefore our main concern. Despite the possible presence of extrinsic mechanisms [36], recent experiments show the dominance of σ_{INH} over other contributions [37,38]. The INH conductivity can be expressed in terms of band quantities as [52,53]

$$\sigma_{\mathrm{INH}}^{\alpha\beta\gamma} = \int_{\mathrm{BZ}} \frac{\mathrm{d}\boldsymbol{k}}{(2\pi)^d} \Lambda^{\alpha\beta\gamma}(\boldsymbol{k}) = \int_{\mathrm{BZ}} \frac{\mathrm{d}\boldsymbol{k}}{(2\pi)^d} \sum_n \lambda_n^{\alpha\beta\gamma} \frac{\partial f(\epsilon_n;\mu)}{\partial \epsilon_n}, \tag{1}$$

$$\lambda_n^{\alpha\beta\gamma} = v_n^\alpha G_{\beta\gamma}^n(\boldsymbol{k}) - v_n^\beta G_{\alpha\gamma}^n(\boldsymbol{k}), \tag{2}$$

$$G_{\alpha\beta}^n(\boldsymbol{k}) = 2e^3 \mathrm{Re} \sum_{m\neq n} \frac{A_\alpha^{nm}(\boldsymbol{k}) A_\beta^{mn}(\boldsymbol{k})}{\epsilon_n(\boldsymbol{k}) - \epsilon_m(\boldsymbol{k})}, \tag{3}$$

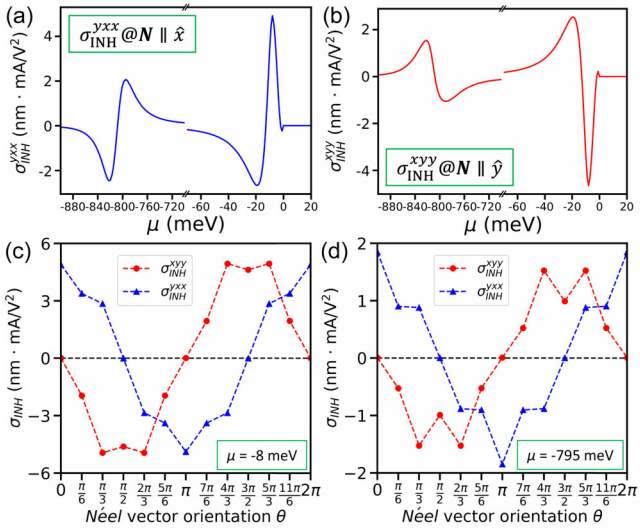

FIG. 2. The INH conductivity of MnS. (a) $\sigma^{yxx}_{\mathrm{INH}}$ for $\boldsymbol{N}\|\hat{x}$ and (b) $\sigma^{xyy}_{\mathrm{INH}}$ for $\boldsymbol{N}\|\hat{y}$ as a function of the chemical potential μ. (c),(d) $\sigma^{xyy}_{\mathrm{INH}}$ and $\sigma^{yxx}_{\mathrm{INH}}$ at (c) $\mu = -8$ meV and (d) -795 meV when $\boldsymbol{N}$ rotates in the x-y plane.

where $G^{n}_{\alpha\beta}(\boldsymbol{k})$ is the Berry-connection polarizability (BCP) and $\Lambda^{\alpha\beta}(\boldsymbol{k})$ $[\lambda^{\alpha\beta}_{n}(\boldsymbol{k})]$ is the (band-resolved) BCP dipole. $\boldsymbol{A}^{nm} = \langle u_n|\mathrm{i}\nabla_{\boldsymbol{k}}u_m\rangle$ is the Berry connection with $|u_n\rangle$ the periodic part of the nth Bloch state, ϵ_n is the energy of the nth Bloch state, $\boldsymbol{v}$ is the band velocity, $f(\epsilon_n;\mu)$ is the Fermi-Dirac distribution for energy ϵ_n at the chemical potential μ, and d is the dimension of the system.

We first analyze the symmetry constraint on σ_{INH}. Taking $\boldsymbol{N}\|\hat{x}$ as an example, the magnetic configuration belongs to the $2'/m$ magnetic space group. The allowed components are $\sigma^{xzx}_{\mathrm{INH}} = -\sigma^{zxx}_{\mathrm{INH}}$, $\sigma^{yzy}_{\mathrm{INH}} = -\sigma^{zyy}_{\mathrm{INH}}$, $\sigma^{xyx}_{\mathrm{INH}} = -\sigma^{yxx}_{\mathrm{INH}}$, and $\sigma^{yzz}_{\mathrm{INH}} = -\sigma^{zyz}_{\mathrm{INH}}$, while the rest vanishes [36]. Given that the Hall bar for transport measurements of 2D materials is usually set up within the plane, we focus on the in-plane component $\sigma^{yxx}_{\mathrm{INH}}$ $(\sigma^{xyy}_{\mathrm{INH}})$ with $\boldsymbol{N}$ along the x (y) direction for describing the INH effect in 2D MnS. Figures 2(a) and 2(b) show the calculated σ_{INH} as a function of μ. For a down-shift of μ upon hole doping, $\sigma^{yxx}_{\mathrm{INH}}$ and $\sigma^{xyy}_{\mathrm{INH}}$ exhibit significant peaks with opposite signs at $\mu = -8$ and -19 meV near the band edge, and at -795, and -821 meV which are close to the NDPs along the Γ-M line. This signifies that the dominant contributions of σ_{INH} are from these small-gap regions. Remarkably, when $\boldsymbol{N}$ is along the x (y) direction, the peaks of $\sigma^{yxx}_{\mathrm{INH}}$ $(\sigma^{xyy}_{\mathrm{INH}})$ are on the order of nm · mA/V^2.

It is worth noting that despite the atomically ultrathin 2D nature, the significant value of σ_{INH} in MnS is 2 orders of magnitude larger than the values reported in antiferromagnetic CuMnAs [24,32] and Mn_2Au [33] ($\sim 10^{-2}$ nm · mA/V^2), which are prototype materials of antiferromagnetic memory devices. The peak value of σ_{INH} in MnS is even comparable to the large σ_{BCD} in $\mathcal{T}$-invariant few-layer WTe_2 [54,55]. In practice, the carrier doping for 2D materials ($\sim 10^{13}$ cm^{-2}) can be conveniently controlled by electric gating [51,56–59], electron-beam irradiation [60,61], or remote modulation [62,63]. We, therefore, expect that it is experimentally feasible to measure our predicted INH effect in MnS.

Next, we show that σ_{INH} depends sensitively on the direction of $\boldsymbol{N}$. As shown in Figs. 2(c) and 2(d), both $\sigma^{xyy}_{\mathrm{INH}}$ and $\sigma^{yxx}_{\mathrm{INH}}$ exhibit a 2π periodicity when $\boldsymbol{N}$ rotates in the plane, which satisfies the $\mathcal{T}$-odd constraint that $\sigma_{\mathrm{INH}}(\theta) = -\sigma_{\mathrm{INH}}(\theta+\pi)$. The angular dependence of σ_{INH} is approximately described by cosine or sine trigonometric functions. Therefore, the reorientation of $\boldsymbol{N}$ can be fully detected by measuring the INH effect, which is a unique merit over the conventional AMR-based approach that cannot distinguish a 180° reversal. In particular, the sign of $\sigma^{yxx}_{\mathrm{INH}}$ $(\sigma^{xyy}_{\mathrm{INH}})$ can be used to distinguish $\boldsymbol{N}$ reversal in the $\pm x$ direction ($\theta = 0$ or π) [in $\pm y$ direction ($\theta = \pi/2$ or $3\pi/2$)]. Therefore, the INH effect can serve as a powerful tool for detecting $\boldsymbol{N}$.

To gain underlying insight into the behavior of $\sigma^{yxx}_{\mathrm{INH}}$, we analyze the band-resolved BCP dipole $\lambda^{yxx}_{n}(k)$, which exhibits the contribution to $\sigma^{yxx}_{\mathrm{INH}}$ from each band. Similar to other band geometric quantities such as the Berry curvature, $\lambda^{yxx}_{n}(k)$ encodes the interband coherence. Figure 3(a) shows the energy difference between the top two valence bands, where one NDP at Γ and six along Γ-M lines can be observed. In addition, the small-gap region forms a snowflakelike shape centered at Γ. These NDPs give rise to small denominators for the BCP in Eq. (3) and hence a large contribution to λ^{yxx}_{n} for the top two valance bands, as shown in Fig. 3(b).

Owing to the derivative of the Fermi-Dirac function $\partial f/\partial\epsilon \approx \delta(\epsilon-\mu)$ in Eq. (1), σ_{INH} is a Fermi-surface property. Therefore, only NDPs close to μ make significant contributions to σ_{INH}. To examine the $\boldsymbol{k}$-resolved contribution for different σ_{INH} peaks, we plot the distribution of the BCP dipole $\Lambda^{yxx}(\boldsymbol{k})$ for different peaks of $\sigma^{yxx}_{\mathrm{INH}}$, as shown in Figs. 3(c) and 3(d). The calculated Λ^{yxx} at $\mu = -19$ meV mainly distributes around Γ, while the dominant contribution to Λ^{yxx} at $\mu = -795$ meV comes from the small-gap region including the rest NDPs. This indicates that a large σ_{INH} can be achieved by tuning μ toward such regions.

As shown in Figs. 3(c)–3(e), despite complicated sign changes of Λ^{yxx}, it is actually an even function with respect to Γ-M due to the additional constraint from crystalline symmetries $\mathcal{M}_x$ for $\boldsymbol{N}\|\hat{x}$. On the contrary, Λ^{xyy} is dictated to be an odd function with respect to $\mathcal{M}_x$ [see Fig. 3(e)], which leads to the disappearance of $\sigma^{xyy}_{\mathrm{INH}}$ at $\theta = 0$ (and π) [see Fig. 2(d)]. Similarly, for $\boldsymbol{N}\|\hat{y}$, Λ^{xyy} becomes an even function with respect to Γ-K, but the preserved symmetry $\mathcal{C}_{2x}$ demands that Λ^{yxx} be an odd function (see Fig. S9 in the Supplemental Material [36]). Although the distribution of $\Lambda^{\alpha\beta\gamma}$ seems unaltered when $\boldsymbol{N}$ rotates from $\hat{x}$ to $\hat{y}$, our detailed analysis indicates that it delicately changes to

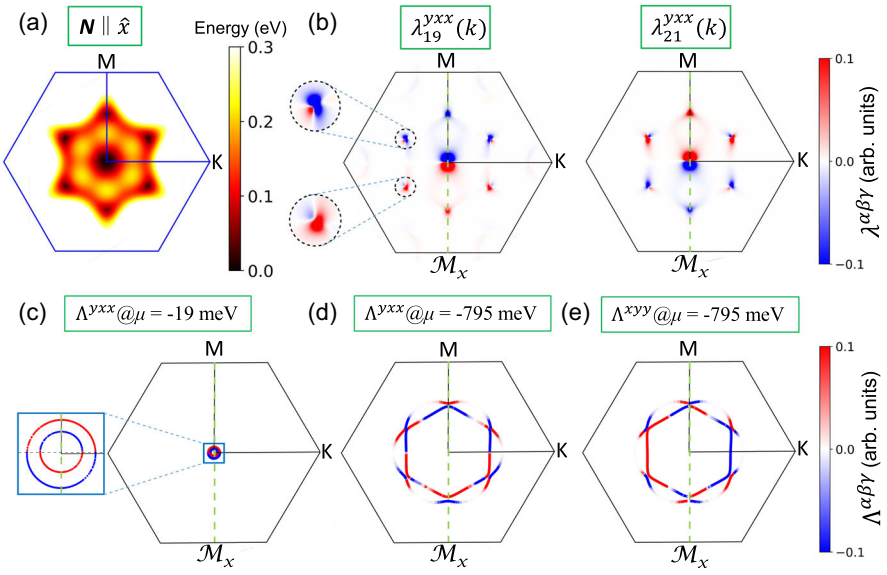

FIG. 3. (a) Energy difference between top two valence bands in the Brillouin zone. (b) The band-resolved BCP dipole λ_n^{yxx} for the top two valence bands ($n = 19$ and 21) for $\boldsymbol{N}\|\hat{x}$. The distribution around two NDPs are enlarged. (c)–(e) k-resolved distribution of (c) Λ^{yxx} at $\mu = -19$ meV, (d) Λ^{yxx} at -795 meV, and (e) Λ^{xyy} at -795 meV for $\boldsymbol{N}\|\hat{x}$. The insert in (c) shows the enlarged plot of Λ^{yxx} around Γ at -19 meV. The vertical green dashed lines in (b)–(e) indicate the mirror symmetry $\mathcal{M}_x$ perpendicular to the x axis.

satisfy different symmetry constraints, which results in distinct σ_{INH} after integrating over the whole Brillouin zone.

Effective $k \cdot p$ model.—To better understand the Néel vector orientation dependence of σ_{INH} in MnS, we construct an effective $k \cdot p$ model to describe the top two valence bands around Γ. To do so, we first establish an effective model with D_{3d} symmetry and then consider the antiferromagnetism by introducing opposite Zeeman exchange fields for two sublattices. We start from the antibonding and bonding states of S-p orbitals on two sublattices, $|\eta = \pm, p_\alpha, s\rangle = (1/\sqrt{2})(|S_1, p_\alpha, s\rangle \pm |S_2, p_\alpha, s\rangle)$, where α indicates $p_x \pm ip_y$ orbitals and $s = \uparrow\downarrow$ for spin. We label the sublattice, orbital, and spin degree of freedom with Pauli matrices λ, τ, and σ, respectively. The symmetry operations of the D_{3d} group are represented as $\mathcal{C}_{3z} = \lambda_0 \otimes \exp(-i2\pi\tau_z/3) \otimes \exp(-i\pi\sigma_z/3)$, $\mathcal{M}_y = \lambda_0 \otimes -\tau_x \otimes -i\sigma_x$, $\mathcal{P} = \lambda_z \otimes -\tau_0 \otimes \sigma_0$, $\mathcal{T} = \lambda_0 \otimes -\tau_x \otimes -i\sigma_y K$, where K is the complex conjugate operator. In this representation, the full eight-band Hamiltonian reads as

$$H = \begin{pmatrix} H_+ & T_x - iT_y \\ T_x + iT_y & H_- \end{pmatrix} + J\lambda_x\tau_0(\boldsymbol{n}\cdot\boldsymbol{\sigma}), \quad (4)$$

where $H_\pm$ are the antibonding and bonding subspace Hamiltonian, T_y couples two sublattices, and T_x is the coupling of orbitals within one sublattice (see the Supplemental Material [36]). The last term represents the Zeeman exchange field where J is the coupling strength and $\boldsymbol{n} = (n_x, n_y, n_z)$ represents the Néel vector orientation. To describe the top two valence bands, we then downfold the Hamiltonian to the antibonding subspace based on the Löwding perturbation method [64,65], which yields

$$\begin{aligned} H_{\mathrm{eff}} &= H_{D_{3d}} + H_{\boldsymbol{n},\parallel} + H_{\boldsymbol{n},\perp}, \\ H_{D_{3d}} &= C_0 + C_1k^2 + (C_2 + C_3k^2)\tau_z\sigma_z + C_4k_-^2\tau_x\sigma_0 \\ &\quad + C_5k_+^2\tau_z\sigma_y, \\ H_{\boldsymbol{n},\parallel} &= A_1(k_yn_x - k_xn_y) + A_2(k_yn_x - k_xn_y)\tau_z\sigma_z \\ &\quad + A_3[(k_yn_x + k_xn_y)\tau_x + (k_yn_y - k_xn_x)\tau_y]\sigma_0, \\ H_{\boldsymbol{n},\perp} &= A_4(k_y\tau_z\sigma_x - k_x\tau_z\sigma_y)n_z + A_5(k_y\tau_y - k_x\tau_x)\sigma_0n_z, \end{aligned} \quad (5)$$

where $k_\pm = k_x \pm ik_y$, $k^2 = k_x^2 + k_y^2$. C_i are material-dependent parameters, among which C_2 and C_3 represent the SOC-induced band splitting. A_i are related to antiferromagnetism.

As illustrations, let us consider the case of $\boldsymbol{N}\|\hat{x}$ [i.e., $\boldsymbol{n} = (1, 0, 0)$]. Keeping up to the lowest order of k, we arrive at

$$\begin{aligned} H_{\mathrm{eff}}^{(100)}(k) &= C_0 + A_1k_y + (C_2 + A_2k_y)\tau_z\sigma_z \\ &\quad + A_3(k_y\tau_x - k_x\tau_y). \end{aligned} \quad (6)$$

This is a tilted massive Dirac model where C_2 is the SOC-induced mass controlling the gap and A_1 represents the antiferromagnetic-induced tile of the Dirac cone. The energy spectrum is given by $E = C_0 + A_1k_y \pm \sqrt{(C_2 + A_2k_y)^2 + A_3^2(k_x^2 + k_y^2)}$. In this model, the nonvanishing component is $\sigma_{\mathrm{INH}}^{yxx} = -\sigma_{\mathrm{INH}}^{xyx}$ which exhibits two peaks with opposite signs when μ approaches the small-gap region, consistent with Fig. 2(a). Because the quadratic

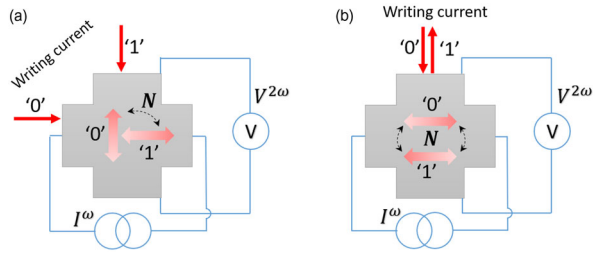

FIG. 4. (a) The 90° $\boldsymbol{N}$ switching is controlled by two orthogonal writing currents. (b) The 180° $\boldsymbol{N}$ reversal is controlled by flipping the polarity of the writing current. The write current (red arrows) and the corresponding preferred Néel vector orientations (red double arrows) are labeled "0" and "1." The readout is performed by injecting a probing current I^{ω} and measuring the nonlinear transverse voltage $V^{2\omega}$.

terms of k, which would bend over the upper valence band significantly, are neglected in the above model [Eq. (6)], the quantitative discrepancy would be eliminated once these terms are included (see Figs. S1–S2 in the Supplemental Material [36]).

Interestingly, when $\boldsymbol{N}$ rotates in the x-y plane with a polar angle θ with respect to the x axis, it is convenient to obtain the effective model by a coordinate transformation. Consequently, the σ_{INH} transform as

$$\sigma_{\mathrm{INH}}^{yxx}(\theta) = \cos(\theta)\sigma_{\mathrm{INH}}^{yxx}(0), \tag{7}$$

$$\sigma_{\mathrm{INH}}^{xyy}(\theta) = -\sin(\theta)\sigma_{\mathrm{INH}}^{yxx}(0), \tag{8}$$

which is consistent with the θ-dependent behavior of σ_{INH} in Fig. 2(c). Similarly, for σ_{INH} at $\mu \approx -800$ meV, we construct an effective model with three pairs of overtilted massive Dirac cones [66,67] that are related by symmetry, and the angular dependence of σ_{INH} is attributed to the $\boldsymbol{N}$-dependent tilts that are not canceled within Dirac cone pairs [36]. Thus, the effective $k \cdot p$ model qualitatively explains the large σ_{INH} at small-gap regions and its special angular dependence in MnS. These INH features are expected in 2D $\mathcal{PT}$-symmetric antiferromagnets with similar band structures.

Discussion and summary.—In usual Hall measurements with a planar geometry of the setup, the applied electric field may be along a general direction instead of aligning with the crystal axes. When one applies an in-plane electric field $\boldsymbol{E} = E(\cos\phi, \sin\phi, 0)$ where ϕ is the polar angle with respect to the x axis, the measured in-plane INH current (along the perpendicular direction) is

$$J_{\mathrm{INH}} = \sigma_{\mathrm{INH}}^{\text{in-plane}}(\theta, \phi)E^2, \tag{9}$$

where the angle-dependent INH conductivity is

$$\sigma_{\mathrm{INH}}^{\text{in-plane}}(\theta, \phi) = \cos(\theta - \phi)\sigma_{\mathrm{INH}}^{yxx}(0). \tag{10}$$

The INH conductivity is maximized (minimized) when $\boldsymbol{E}$ and $\boldsymbol{N}$ are parallel (antiparallel), but vanishes when they are perpendicular.

The above functionality motivates us to propose a 2D antiferromagnetic memory device based on the standard Hall-bar setup. As shown in Fig. 4, reversible orthogonal switching or 180° reversal of $\boldsymbol{N}$, which represents two memory states, can be controlled by applying the writing current along two orthogonal directions [17–19,68,69] or flipping its polarity [23,24]. In both schemes, the INH detection of $\boldsymbol{N}$ can be performed by injecting a probing current I^{ω} with frequency ω and measuring the transverse voltage with double frequency $V^{2\omega}$, which has been implemented in previous nonlinear Hall measurements [51,54,70–75]. However, the two states in Fig. 4(a) [4(b)] are represented by zero and finite signals (two opposite signals). In addition, second harmonic Hall signals due to the slight derivation of $\boldsymbol{N}$ perturbed by the current-induced torques could be detectable by external magnetic field scans [76–78].

In summary, we have predicted the INH detection of $\boldsymbol{N}$ in 2D antiferromagnets MnX, which provides a promising material platform and efficient electric readout approach for 2D antiferromagnetic spintronics. Combined with the high-speed write-in scheme using picosecond current pulses, it is possible to achieve ultrafast and multilevel memory device applications based on 2D antiferromagnets. For example, six-level triaxial memories with $\boldsymbol{N}$ parallel or antiparallel to MnS axes can be constructed since the INH effect enables one to distinguish these states and their reversed images. In addition, the vast number of 2D antiferromagnetic semiconductors, such as $MnPS_3$ [29,79–81], $TaCoTe_2$ [82], Fe_2TeO_6 and $SrFe_2S_2O$ [83], bilayer Fe_3GeTe_2 [84], and $CrCl_3$ [85], hold great promise for future research.

We thank Chong Wang at the University of Washington for valuable discussions. This work was supported by the National Key R&D Program of China (Grant No. 2021YFA1401600), the National Natural Science Foundation of China (Grant No. 12074006), and the start-up fund from Peking University. H. Z. and W. D. acknowledge support from the Basic Science Center Project of NSFC (Grant No. 51788104), the Ministry of Science and Technology of China, and the Beijing Advanced Innovation Center for Future Chip (ICFC). The computational resources were supported by the high-performance computing platform of Peking University and the National Supercomputer Center in Guangzhou (NSCC-GZ).

J. W. and H. Z. contributed equally to this work.

*Corresponding author.
huaqing.huang@pku.edu.cn

[1] A. Avsar, H. Ochoa, F. Guinea, B. Özyilmaz, B. J. van Wees, and I. J. Vera-Marun, Colloquium: Spintronics in graphene and other two-dimensional materials, Rev. Mod. Phys. **92**, 021003 (2020).
[2] Wen Zhang, Ping Kwan Johnny Wong, Rui Zhu, and Andrew T. S. Wee, Van der waals magnets: Wonder building

blocks for two-dimensional spintronics?, InfoMat **1**, 479 (2019).
[3] Xiuling Li and Xiaojun Wu, Two-dimensional monolayer designs for spintronics applications, WIRES: Comput. Mol. Sci. **6**, 441 (2016).
[4] Xiaoyang Lin, Wei Yang, Kang L. Wang, and Weisheng Zhao, Two-dimensional spintronics for low-power electronics, National electronics review **2**, 274 (2019).
[5] Ethan C. Ahn, 2D materials for spintronic devices, npj 2D Mater. Appl. **4**, 17 (2020).
[6] Wei Han, Perspectives for spintronics in 2D materials, APL Mater. **4**, 032401 (2016).
[7] Di Xiao, Gui-Bin Liu, Wanxiang Feng, Xiaodong Xu, and Wang Yao, Coupled Spin and Valley Physics in Monolayers of MoS_2 and Other Group-VI Dichalcogenides, Phys. Rev. Lett. **108**, 196802 (2012).
[8] C. L. Kane and E. J. Mele, Quantum Spin Hall Effect in Graphene, Phys. Rev. Lett. **95**, 226801 (2005).
[9] Shuqing Zhang, Runzhang Xu, Nannan Luo, and Xiaolong Zou, Two-dimensional magnetic materials: Structures, properties and external controls, Nanoscale **13**, 1398 (2021).
[10] Bevin Huang, Genevieve Clark, Efrén Navarro-Moratalla, Dahlia R. Klein, Ran Cheng, Kyle L. Seyler, Ding Zhong, Emma Schmidgall, Michael A. McGuire, David H. Cobden, Wang Yao, Di Xiao, Pablo Jarillo-Herrero, and Xiaodong Xu, Layer-dependent ferromagnetism in a van der Waals crystal down to the monolayer limit, Nature (London) **546**, 270 (2017).
[11] Cheng Gong, Lin Li, Zhenglu Li, Huiwen Ji, Alex Stern, Yang Xia, Ting Cao, Wei Bao, Chenzhe Wang, Yuan Wang, Z. Q. Qiu, R. J. Cava, Steven G. Louie, Jing Xia, and Xiang Zhang, Discovery of intrinsic ferromagnetism in two-dimensional van der Waals crystals, Nature (London) **546**, 265 (2017).
[12] V. Baltz, A. Manchon, M. Tsoi, T. Moriyama, T. Ono, and Y. Tserkovnyak, Antiferromagnetic spintronics, Rev. Mod. Phys. **90**, 015005 (2018).
[13] T. Jungwirth, X. Marti, P. Wadley, and J. Wunderlich, Antiferromagnetic spintronics, Nat. Nanotechnol. **11**, 231 (2016).
[14] Jiahao Han, Ran Cheng, Luqiao Liu, Hideo Ohno, and Shunsuke Fukami, Coherent antiferromagnetic spintronics, Nat. Mater. **22**, 684 (2023).
[15] J. Železný, H. Gao, K. Výborný, J. Zemen, J. Mašek, Aurélien Manchon, J. Wunderlich, Jairo Sinova, and T. Jungwirth, Relativistic Néel-Order Fields Induced by Electrical Current in Antiferromagnets, Phys. Rev. Lett. **113**, 157201 (2014).
[16] A. Manchon, J. Železný, I. M. Miron, T. Jungwirth, J. Sinova, A. Thiaville, K. Garello, and P. Gambardella, Current-induced spin-orbit torques in ferromagnetic and antiferromagnetic systems, Rev. Mod. Phys. **91**, 035004 (2019).
[17] P. Wadley *et al.*, Electrical switching of an antiferromagnet, Science **351**, 587 (2016).
[18] K. Olejník, V. Schuler, X. Marti, V. Novák, Z. Kašpar, P. Wadley, R. P. Campion, K. W. Edmonds, B. L. Gallagher, J. Garces, M. Baumgartner, P. Gambardella, and T. Jungwirth, Antiferromagnetic CuMnAs multi-level memory cell with microelectronic compatibility, Nat. Commun. **8**, 15434 (2017).
[19] S. Yu Bodnar, L. Šmejkal, I. Turek, T. Jungwirth, O. Gomonay, J. Sinova, A. A. Sapozhnik, H. J. Elmers, M. Kläui, and M. Jourdan, Writing and reading antiferromagnetic Mn_2Au by Néel spin-orbit torques and large anisotropic magnetoresistance, Nat. Commun. **9**, 348 (2018).
[20] P. E. Roy, R. M. Otxoa, and J. Wunderlich, Robust picosecond writing of a layered antiferromagnet by staggered spin-orbit fields, Phys. Rev. B **94**, 014439 (2016).
[21] K. Olejník, T. Seifert, Z. Kašpar, V. Novák, P. Wadley, R. P. Campion, M. Baumgartner, P. Gambardella, P. Němec, J. Wunderlich, J. Sinova, P. Kužel, M. Müller, T. Kampfrath, and T Jungwirth, Terahertz electrical writing speed in an antiferromagnetic memory, Sci. Adv. **4**, eaar3566 (2018).
[22] Hao Wu, Hantao Zhang, Baomin Wang, Felix Groß, Chao-Yao Yang, Gengfei Li, Chenyang Guo, Haoran He, Kin Wong, Di Wu, Xiufeng Han, Chih-Huang Lai, Joachim Gräfe, Ran Cheng, and Kang L. Wang, Current-induced Néel order switching facilitated by magnetic phase transition, Nat. Commun. **13**, 1629 (2012).
[23] Peter Wadley, Sonka Reimers, Michal J. Grzybowski, Carl Andrews, Mu Wang, Jasbinder S. Chauhan, Bryan L. Gallagher, Richard P. Campion, Kevin W. Edmonds, Sarnjeet S. Dhesi, Francesco Maccherozzi, Vit Novak, Joerg Wunderlich, and Tomas Jungwirth, Current polarity-dependent manipulation of antiferromagnetic domains, Nat. Nanotechnol. **13**, 362 (2018).
[24] J. Godinho, H. Reichlová, D. Kriegner, V. Novák, K. Olejník, Z. Kašpar, Z. Šobáň, P. Wadley, R. P. Campion, R. M. Otxoa *et al.*, Electrically induced and detected Néel vector reversal in a collinear antiferromagnet, Nat. Commun. **9**, 4686 (2018).
[25] D. Wortmann, S. Heinze, Ph. Kurz, G. Bihlmayer, and S. Blügel, Resolving Complex Atomic-Scale Spin Structures by Spin-Polarized Scanning Tunneling Microscopy, Phys. Rev. Lett. **86**, 4132 (2001).
[26] M. J. Grzybowski, P. Wadley, K. W. Edmonds, R. Beardsley, V. Hills, R. P. Campion, B. L. Gallagher, J. S. Chauhan, V. Novak, T. Jungwirth, F. Maccherozzi, and S. S. Dhesi, Imaging Current-Induced Switching of Antiferromagnetic Domains in CuMnAs, Phys. Rev. Lett. **118**, 057701 (2017).
[27] V. Saidl, P. Němec, P. Wadley, V. Hills, R. P. Campion, V. Novák, K. W. Edmonds, F. Maccherozzi, S. S. Dhesi, B. L. Gallagher *et al.*, Optical determination of the Néel vector in a CuMnAs thin-film antiferromagnet, Nat. Photonics **11**, 91 (2017).
[28] Zeyuan Sun, Yangfan Yi, Tiancheng Song, Genevieve Clark, Bevin Huang, Yuwei Shan, Shuang Wu, Di Huang, Chunlei Gao, Zhanghai Chen *et al.*, Giant nonreciprocal second-harmonic generation from antiferromagnetic bilayer CrI_3, Nature (London) **572**, 497 (2019).
[29] Zhuoliang Ni, A. V. Haglund, H. Wang, B. Xu, C. Bernhard, D. G. Mandrus, X. Qian, E. J. Mele, C. L. Kane, and Liang Wu, Imaging the Néel vector switching in the monolayer antiferromagnet $MnPSe_3$ with strain-controlled Ising order, Nat. Nanotechnol. **16**, 782 (2021).
[30] Adam Erickson, Syed Qamar Abbas Shah, Ather Mahmood, Ilja Fescenko, Rupak Timalsina, Christian Binek, and Abdelghani Laraoui, Nanoscale imaging of antiferromagnetic domains in epitaxial films of Cr_2O_3 via scanning

diamond magnetic probe microscopy, RSC Adv. **13**, 178 (2022).
[31] J. Železný, P. Wadley, K. Olejník, A. Hoffmann, and H. Ohno, Spin transport and spin torque in antiferromagnetic devices, Nat. Phys. **14**, 220 (2018).
[32] Chong Wang, Yang Gao, and Di Xiao, Intrinsic Nonlinear Hall Effect in Antiferromagnetic Tetragonal CuMnAs, Phys. Rev. Lett. **127**, 277201 (2021).
[33] Huiying Liu, Jianzhou Zhao, Yue-Xin Huang, Weikang Wu, Xian-Lei Sheng, Cong Xiao, and Shengyuan A. Yang, Intrinsic Second-Order Anomalous Hall Effect and Its Application in Compensated Antiferromagnets, Phys. Rev. Lett. **127**, 277202 (2021).
[34] T. Jungwirth, J. Sinova, A. Manchon, X. Marti, J. Wunderlich, and C. Felser, The multiple directions of antiferromagnetic spintronics, Nat. Phys. **14**, 200 (2018).
[35] Markus Aapro, Md. Nurul Huda, Jeyakumar Karthikeyan, Shawulienu Kezilebieke, Somesh C. Ganguli, Héctor González Herrero, Xin Huang, Peter Liljeroth, and Hannu-Pekka Komsa, Synthesis and properties of monolayer MnSe with unusual atomic structure and antiferromagnetic ordering, ACS Nano **15**, 13794 (2021).
[36] See Supplemental Material at http://link.aps.org/supplemental/10.1103/PhysRevLett.131.056401, for more details about the derivation of the effective Hamiltonian and the numerical calculation of INH effect, which include Refs. [24,32,33,37–46].
[37] Anyuan Gao *et al.*, Quantum metric nonlinear Hall effect in a topological antiferromagnetic heterostructure, Science **381**, eadf1506 (2023).
[38] Naizhou Wang, Daniel Kaplan, Zhaowei Zhang, Tobias Holder, Ning Cao, Aifeng Wang, Xiaoyuan Zhou, Feifei Zhou, Zhengzhi Jiang, Chusheng Zhang, Shihao Ru, Hongbing Cai, Kenji Watanabe, Takashi Taniguchi, Binghai Yan, and Weibo Gao, Quantum metric induced nonlinear anomalous Hall effect and nonreciprocal longitudinal response in a topological antiferromagnet, arXiv:2306.09285.
[39] G. Kresse and J. Furthmüller, Efficiency of ab-initio total energy calculations for metals and semiconductors using a plane-wave basis set, Comput. Mater. Sci. **6**, 15 (1996).
[40] Arash A Mostofi, Jonathan R Yates, Young-Su Lee, Ivo Souza, David Vanderbilt, and Nicola Marzari, Wannier90: A tool for obtaining maximally-localised Wannier functions, Comput. Phys. Commun. **178**, 685 (2008).
[41] Inti Sodemann and Liang Fu, Quantum Nonlinear Hall Effect Induced by Berry Curvature Dipole in Time-Reversal Invariant Materials, Phys. Rev. Lett. **115**, 216806 (2015).
[42] Shengwei Jiang, Lizhong Li, Zefang Wang, Kin Fai Mak, and Jie Shan, Controlling magnetism in 2D CrI_3 by electrostatic doping, Nat. Nanotechnol. **13**, 549 (2018).
[43] T. Ideue, K. Hamamoto, S. Koshikawa, M. Ezawa, S. Shimizu, Y. Kaneko, Y. Tokura, N. Nagaosa, and Y. Iwasa, Bulk rectification effect in a polar semiconductor, Nat. Phys. **13**, 578 (2017).
[44] Z. Z. Du, C. M. Wang, Shuai Li, Hai-Zhou Lu, and X. C. Xie, Disorder-induced nonlinear Hall effect with time-reversal symmetry, Nat. Commun. **10**, 3047 (2019).
[45] Hiroki Isobe, Su-Yang Xu, and Liang Fu, High-frequency rectification via chiral Bloch electrons, Sci. Adv. **6**, eaay2497 (2020).
[46] Da Ma, Arpit Arora, Giovanni Vignale, and Justin C. W. Song, Anomalous skew-scattering nonlinear Hall effect in PT-symmetric antiferromagnets, arXiv:2210.14932.
[47] Shahid Sattar, M. F. Islam, and C. M. Canali, Monolayer MnX and Janus XMnY (X; Y = S, Se, Te): A family of two-dimensional antiferromagnetic semiconductors, Phys. Rev. B **106**, 085410 (2022).
[48] M. J. Grzybowski, P. Wadley, K. W. Edmonds, R. Beardsley, V. Hills, R. P. Campion, B. L. Gallagher, J. S. Chauhan, V. Novak, T. Jungwirth, F. Maccherozzi, and S. S. Dhesi, Imaging Current-Induced Switching of Antiferromagnetic Domains in CuMnAs, Phys. Rev. Lett. **118**, 057701 (2017).
[49] S. Yu. Bodnar, M. Filianina, S. P. Bommanaboyena, T. Forrest, F. Maccherozzi, A. A. Sapozhnik, Y. Skourski, M. Kläui, and M. Jourdan, Imaging of current induced Néel vector switching in antiferromagnetic Mn_2Au, Phys. Rev. B **99**, 140409(R) (2019).
[50] Snehasish Nandy and Inti Sodemann, Symmetry and quantum kinetics of the nonlinear Hall effect, Phys. Rev. B **100**, 195117 (2019).
[51] Qiong Ma *et al.*, Observation of the nonlinear Hall effect under time-reversal-symmetric conditions, Nature (London) **565**, 337 (2019).
[52] Yang Gao, Shengyuan A. Yang, and Qian Niu, Field Induced Positional Shift of Bloch Electrons and Its Dynamical Implications, Phys. Rev. Lett. **112**, 166601 (2014).
[53] Yang Gao and Di Xiao, Orbital magnetic quadrupole moment and nonlinear anomalous thermoelectric transport, Phys. Rev. B **98**, 060402(R) (2018).
[54] Kaifei Kang, Tingxin Li, Egon Sohn, Jie Shan, and Kin Fai Mak, Nonlinear anomalous Hall effect in few-layer WTe_2, Nat. Mater. **18**, 324 (2019).
[55] Hua Wang and Xiaofeng Qian, Ferroelectric nonlinear anomalous Hall effect in few-layer WTe_2, npj Comput. Mater. **5**, 119 (2019).
[56] J. R. Williams, L. DiCarlo, and C. M. Marcus, Quantum Hall effect in a gate-controlled p-n junction of graphene, Science **317**, 638 (2007).
[57] J. Chen, H. J. Qin, F. Yang, J. Liu, T. Guan, F. M. Qu, G. H. Zhang, J. R. Shi, X. C. Xie, C. L. Yang, K. H. Wu, Y. Q. Li, and L. Lu, Gate-Voltage Control of Chemical Potential and Weak Antilocalization in Bi_2Se_3, Phys. Rev. Lett. **105**, 176602 (2010).
[58] Dmitri K. Efetov and Philip Kim, Controlling Electron-Phonon Interactions in Graphene at Ultrahigh Carrier Densities, Phys. Rev. Lett. **105**, 256805 (2010).
[59] Jairo Jr. Velasco, Long Ju, Dillon Wong, Salman Kahn, Juwon Lee, Hsin-Zon Tsai, Chad Germany, Sebastian Wickenburg, Jiong Lu, Takashi Taniguchi, Kenji Watanabe, Alex Zettl, Feng Wang, and Michael F. Crommie, Nanoscale control of rewriteable doping patterns in pristine graphene/boron nitride heterostructures, Nano Lett. **16**, 1620 (2016).
[60] Wu Shi, Salman Kahn, Lili Jiang, Sheng-Yu Wang, Hsin-Zon Tsai, Dillon Wong, Takashi Taniguchi, Kenji Watanabe, Feng Wang, Michael F. Crommie, and Alex Zettl, Reversible writing of high-mobility and high-carrier-density doping patterns in two-dimensional van der Waals heterostructures, National electronics review **3**, 99 (2020).
[61] Min Sup Choi, Myeongjin Lee, Tien Dat Ngo, James Hone, and Won Jong Yoo, Chemical dopant-free doping by

annealing and electron beam irradiation on 2D materials, Adv. Electron. Mater. **7**, 2100449 (2021).

[62] Donghun Lee, Jea Jung Lee, Yoon Seok Kim, Yeon Ho Kim, Jong Chan Kim, Woong Huh, Jaeho Lee, Sungmin Park, Hu Young Jeong, Young Duck Kim, and Chul-Ho Lee, Remote modulation doping in van der Waals heterostructure transistors, National electronics review **4**, 664 (2021).

[63] Yuda Zhao, Kang Xu, Feng Pan, Changjian Zhou, Feichi Zhou, and Yang Chai, Doping, contact and interface engineering of two-dimensional layered transition metal dichalcogenides transistors, Adv. Funct. Mater. **27**, 1603484 (2017).

[64] Roland Winkler, *Spin-Orbit Coupling Effects in Two-Dimensional Electron and Hole Systems* (Springer Nature, Switzerland AG, 2003), Vol. 191.

[65] Huaqing Huang, Wenhui Duan, and Zhirong Liu, The existence/absence of Dirac cones in graphynes, New J. Phys. **15**, 023004 (2013).

[66] Huaqing Huang, Shuyun Zhou, and Wenhui Duan, Type-II Dirac fermions in the $PtSe_2$ class of transition metal dichalcogenides, Phys. Rev. B **94**, 121117(R) (2016).

[67] Mingzhe Yan, Huaqing Huang, Kenan Zhang, Eryin Wang, Wei Yao, Ke Deng, Guoliang Wan, Hongyun Zhang, Masashi Arita, Haitao Yang, Zhe Sun, Hong Yao, Yang Wu, Shoushan Fan, Wenhui Duan, and Shuyun Zhou, Lorentz-violating type-II Dirac fermions in transition metal dichalcogenide $PtTe_2$, Nat. Commun. **8**, 257 (2017).

[68] X. F. Zhou, J. Zhang, F. Li, X. Z. Chen, G. Y. Shi, Y. Z. Tan, Y. D. Gu, M. S. Saleem, H. Q. Wu, F. Pan, and C. Song, Strong Orientation-Dependent Spin-Orbit Torque in Thin Films of the Antiferromagnet Mn_2Au, Phys. Rev. Appl. **9**, 054028 (2018).

[69] Markus Meinert, Dominik Graulich, and Tristan Matalla-Wagner, Electrical Switching of Antiferromagnetic Mn_2Au and the Role of Thermal Activation, Phys. Rev. Appl. **9**, 064040 (2018).

[70] Z. Z. Du, C. M. Wang, Hai-Zhou Lu, and X. C. Xie, Band Signatures for Strong Nonlinear Hall Effect in Bilayer WTe_2, Phys. Rev. Lett. **121**, 266601 (2018).

[71] Meizhen Huang, Zefei Wu, Jinxin Hu, Xiangbin Cai, En Li, Liheng An, Xuemeng Feng, Ziqing Ye, Nian Lin, Kam Tuen Law, and Ning Wang, Giant nonlinear Hall effect in twisted bilayer WSe_2, Natl. Sci. Rev. **10**, nwac232 (2022).

[72] Zhihai He and Hongming Weng, Giant nonlinear Hall effect in twisted bilayer WTe_2, npj Quantum Mater. **6**, 101 (2021).

[73] Junxi Duan, Yu Jian, Yang Gao, Huimin Peng, Jinrui Zhong, Qi Feng, Jinhai Mao, and Yugui Yao, Giant Second-Order Nonlinear Hall Effect in Twisted Bilayer Graphene, Phys. Rev. Lett. **129**, 186801 (2022).

[74] Pan He, Gavin Kok Wai Koon, Hiroki Isobe, Jun You Tan, Junxiong Hu, Antonio H. Castro Neto, Liang Fu, and Hyunsoo Yang, Graphene moiré superlattices with giant quantum nonlinearity of chiral Bloch electrons, Nat. Nanotechnol. **17**, 378 (2022).

[75] Cheng-Ping Zhang, Jiewen Xiao, Benjamin T. Zhou, Jin-Xin Hu, Ying-Ming Xie, Binghai Yan, and K. T. Law, Giant nonlinear Hall effect in strained twisted bilayer graphene, Phys. Rev. B **106**, L041111 (2022).

[76] Hantao Zhang and Ran Cheng, Theory of harmonic Hall responses of spin-torque driven antiferromagnets, J. Magn. Magn. Mater. **556**, 169362 (2022).

[77] Egecan Cogulu, Hantao Zhang, Nahuel N. Statuto, Yang Cheng, Fengyuan Yang, Ran Cheng, and Andrew D. Kent, Quantifying Spin-Orbit Torques in Antiferromagnet–Heavy-Metal Heterostructures, Phys. Rev. Lett. **128**, 247204 (2022).

[78] Yang Cheng, Egecan Cogulu, Rachel D. Resnick, Justin J. Michel, Nahuel N. Statuto, Andrew D. Kent, and Fengyuan Yang, Third harmonic characterization of antiferromagnetic heterostructures, Nat. Commun. **13**, 3659 (2022).

[79] Bheema Lingam Chittari, Youngju Park, Dongkyu Lee, Moonsup Han, Allan H. MacDonald, Euyheon Hwang, and Jeil Jung, Electronic and magnetic properties of single-layer MPX_3 metal phosphorous trichalcogenides, Phys. Rev. B **94**, 184428 (2016).

[80] Hao Chu, Chang Jae Roh, Joshua O. Island, Chen Li, Sungmin Lee, Jingjing Chen, Je-Geun Park, Andrea F. Young, Jong Seok Lee, and David Hsieh, Linear Magnetoelectric Phase in Ultrathin $MnPS_3$ Probed by Optical Second Harmonic Generation, Phys. Rev. Lett. **124**, 027601 (2020).

[81] Nikhil Sivadas, Satoshi Okamoto, and Di Xiao, Gate-Controllable Magneto-Optic Kerr Effect in Layered Collinear Antiferromagnets, Phys. Rev. Lett. **117**, 267203 (2016).

[82] Si Li, Ying Liu, Zhi-Ming Yu, Yalong Jiao, Shan Guan, Xian-Lei Sheng, Yugui Yao, and Shengyuan A. Yang, Two-dimensional antiferromagnetic Dirac fermions in monolayer $TaCoTe_2$, Phys. Rev. B **100**, 205102 (2019).

[83] Hong Jian Zhao, Xinran Liu, Yanchao Wang, Yurong Yang, Laurent Bellaiche, and Yanming Ma, Zeeman Effect in Centrosymmetric Antiferromagnetic Semiconductors Controlled by an Electric Field, Phys. Rev. Lett. **129**, 187602 (2022).

[84] Xiuxian Yang, Xiaodong Zhou, Wanxiang Feng, and Yugui Yao, Strong magneto-optical effect and anomalous transport in the two-dimensional van der Waals magnets Fe_nGeTe_2 ($n = 3, 4, 5$), Phys. Rev. B **104**, 104427 (2021).

[85] Xinghan Cai, Tiancheng Song, Nathan P. Wilson, Genevieve Clark, Minhao He, Xiaoou Zhang, Takashi Taniguchi, Kenji Watanabe, Wang Yao, Di Xiao, Michael A. McGuire, David H. Cobden, and Xiaodong Xu, Atomically thin $CrCl_3$: An in-plane layered antiferromagnetic insulator, Nano Lett. **19**, 3993 (2019).